Phase diagram and stability of mixed-cation lead iodide perovskites: A theory and experiment combined study

Zhengwei Xu,[1] Yicheng Zhao,[2,*] Jiyun Zhang,[2,3] Keqiu Chen,[1] Christoph J. Brabec,[2,3] and Yexin Feng[1,4,†]

[1]*Hunan Provincial Key Laboratory of Low-Dimensional Structural Physics and Devices, School of Physics and Electronics, Hunan University, Changsha 410082, China*

[2]*Institute of Materials for Electronics and Energy Technology (i-MEET), Department of Materials Science and Engineering, Friedrich-Alexander-Universität Erlangen-Nürnberg, Martensstrasse 7, 91058 Erlangen, Germany*

[3]*Helmholtz-Institute Erlangen-Nürnberg (HI-ERN), Immerwahrstraße 2, 91058 Erlangen, Germany*

[4]*Department of Materials Science and Engineering, University of Washington, Seattle, Washington 98195, USA*

(Received 20 June 2020; accepted 17 August 2020; published 9 September 2020)

Alloying structurally similar perovskites to form mixed-cation lead iodide perovskites, e.g., $Cs_xFA_{(1-x)}PbI_3$, $MA_xFA_{(1-x)}PbI_3$, and $Cs_xMA_yFA_{(1-x-y)}PbI_3$, could improve the performance of perovskite-based solar cells and light-emitting diodes. However, a phase diagram of them and a clear understanding of the underlying atomic-scale mechanism are still lacking. Using *ab initio* calculations combined with high-throughput experimentation, we demonstrate the phase diagram of mixed-cation lead iodide perovskites. Only a small proportion of monovalent cations ($Cs^+/Rb^+/MA^+$) could be incorporated into the $FAPbI_3/MAPbI_3$ matrix; otherwise it will be separated into δ-$CsPbI_3$, δ-$RbPbI_3$, MAI, etc. The smaller the radius of doping cations, the harder it is to incorporate them into a perovskite lattice and the easier it is to stabilize the perovskite phase. In $FAPbI_3$-based multication perovskites, moreover, over 10 mol % alloying is needed to convert δ phase to α phase at room temperature. The combined upper and lower limits for doping concentration restrict the appropriate alloying ratio to a narrow window. We further plot the relative energy diagram for triple-cation perovskite $Cs_xMA_yFA_{(1-x-y)}PbI_3$, which reveals the ideal doping ratio for uniform stable alloying. This theory-experiment-combined study provides a clear microscopic picture of phase stability and segregation for mixed-cation perovskite solids.

DOI: 10.1103/PhysRevMaterials.4.095401

I. INTRODUCTION

Organic-inorganic halide perovskites (OIHPs) have shown enormous potential for solar cells, with a certified power conversion efficiency (PCE) of around 25% [1]. The excellent performance of perovskite solar cells has been attributed to many factors [2,3], such as strong optical absorption over the visible spectrum [4–6], high defect tolerance [7–9], low-exciton binding energy [10,11], high carrier mobility [12–14], simple manufacturing routes [15,16], tunable chemical composition [17,18], etc.

Among them, composition engineering, especially incorporating different cations into an $FAPbI_3$ lattice, enables a close-to-ideal band gap with low defects [18–20], leading to by far the best OIHP solar cells [21–23]. Moreover, the instability of OIHPs toward light and moisture is a major obstacle to developing long-term photovoltaic devices. Experiments have reported that alloying MA^+, Cs^+, Rb^+, and K^+ into $FAPbI_3$ can improve the phase stability of OIHPs [24–29]. For example, incorporating Rb^+ into $FAPbI_3$ can tune the tolerance factor and stabilize the perovskite phase in ambient air [29,30]. Syzgantseva *et al.* performed a systematic computational study on $MA^+/Cs^+/Rb^+$ doping into $FAPbI_3$ with the doping concentration ranging from 8.3% to 50%. They found that cations like Cs^+ and Rb^+ are more efficient in the stabilization of α-phase OIHPs than MA^+ [27], but it still lacks experimental support.

Although the advantages of mixed-cation OIHPs have been widely recognized, the atomic-scale mechanisms are still vague. Several most fundamental problems, such as "whether or not doping cations could be uniformly incorporated into the perovskite lattice," "What is the byproduct of phase segregation?" and "Is there an optimized mixing ratio for specific cation?" are still under debate. Many experimental works claimed that cations like MA^+, Cs^+, Rb^+, and K^+ could be uniformly embedded into $FAPbI_3$ on the basis of x-ray diffraction (XRD) measurements [24,26]. However, by using the solid-state NMR technique, Kubicki *et al.* have presented a different scenario. For the first time, they showed clear evidence that Cs^+ can take up to 15 mol % of the *A* site of $FAPbI_3$, while there was no proof of Rb^+ or K^+ incorporation into the lattice [31,32]. In another work by Zhang *et al.*, it was found that although Rb^+ doping leads to an improvement in the photovoltaic performance, Rb^+ was not fully embedded in the perovskite lattice [29]. Another experiment also suggested that Rb^+ and Cs^+ dopants could be incorporated to the *A* site, while Li^+, Na^+, and K^+ cannot [33]. Therefore a general investigation on the phase diagram of mixed-cation OIHPs, especially concerning the atomic-scale mechanisms of phase stability and segregation, is urgent.

*yicheng.zhao@fau.de
†yexinfeng@hnu.edu.cn

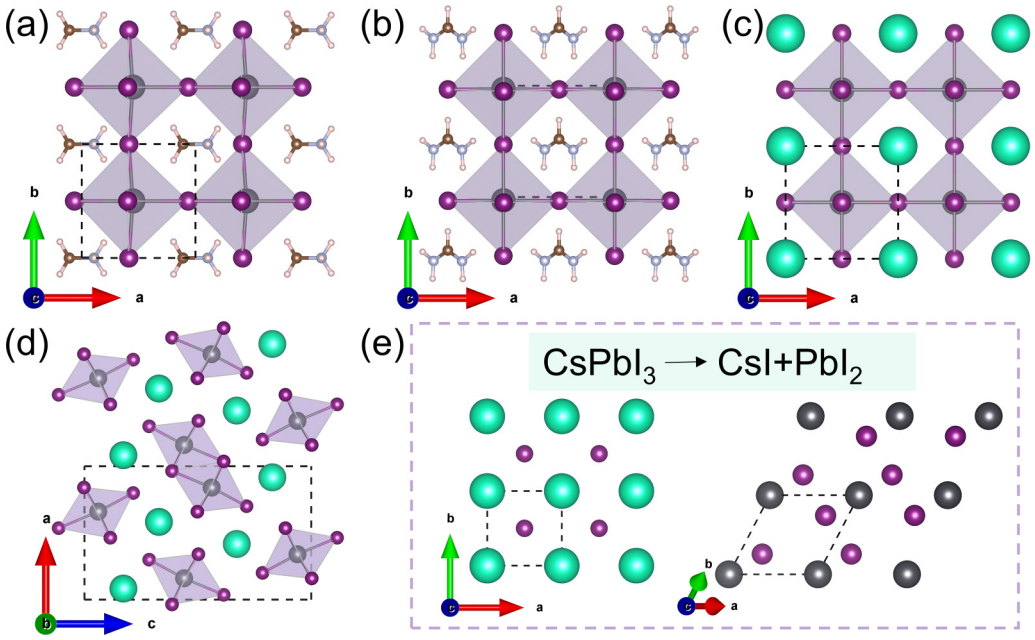

FIG. 1. Atomic structures and computational models. Structures of (a) $MAPbI_3$, (b) $FAPbI_3$, and (c) $CsPbI_3$ with α phase. (d) Nonperovskite phase $CsPbI_3$ (δ-$CsPbI_3$). Structures of (e) CsI and PbI_2, which represent the products of phase segregation $CsPbI_3 \rightarrow CsI + PbI_2$. The green spheres represent the Cs atom. The purple polyhedra represent the octahedral perovskite cage formed by the bonding of the Pb (steel blue) and I (dark purple) atoms. The C, N, and H atoms are represented by brown, light blue, and light pink spheres, respectively.

In this study we report a theory-experiment-combined study on the phase diagram and stability of double- and triple-cation lead iodide perovskites. We find that a small proportion of $Cs^+/Rb^+/MA^+$ could be uniformly incorporated into the perovskite phase of $FAPbI_3/MAPbI_3$. But K^+ cannot be alloyed in $FAPbI_3$, although it can somehow modify the crystallization dynamics to form a metastable perovskite phase. In $FAPbI_3$-based alloy perovskites, over 10 mol % alloying is needed to stabilize the perovskite phase at room temperature, which restricts the appropriate doping concentration to a very narrow region. Cs^+ is more likely to be incorporated into the lattice because its radius is most comparable to those of FA^+ and MA^+. The temperature effects of $FAPbI_3$-based alloys are then discussed from a theoretical perspective by plotting the temperature-composition phase diagram. The relative energy diagram for triple-cation perovskite $Cs_xMA_yFA_{(1-x-y)}PbI_3$ is also further mapped out. The main goal of this study is to determine the doping region (with K, Rb, Cs, and MA) where $FAPbI_3$-based perovskite phase is stable at room temperature. It reveals the ideal doping ratio for uniform mixing and a stable perovskite phase, which is consistent with experimental results. These findings provide deep insights for understanding the phase stability and segregation of mixed-cation lead iodide perovskites.

II. RESULTS AND DISCUSSION

A. Theoretical results of double-cation perovskites

Several experiments demonstrated that excess doping of A^+ (A = Cs, Rb, K, or MA) in mixed-cation perovskite may lead to phase separation with products of α-phase $APbI_3$, δ-phase $APbI_3$, or AI [24,25,34,35]; therefore here we evaluate the relative energies of $A_xB_yFA_{(1-x-y)}PbI_3$ structures compared with a control system (α-$FAPbI_3$) and reference systems as a start. On the basis of the density functional theory (DFT) method, the relative energy for the binary doping system is defined by Eq. (1):

$$E_{\mathrm{rel}} = E(x) - xE_{\mathrm{APbI3}} - (1-x)E_{\mathrm{FA/MAPbI3}}, \qquad (1)$$

where $E(x)$ denotes the total energy of the investigated structure $A_xFA_{(1-x)}PbI_3$ ($A_xMA_{(1-x)}PbI_3$), and $E_{\mathrm{FAPbI3}}(E_{\mathrm{MAPbI3}})$ is the total energy of the pure cubic supercell without doping, as shown in Fig. 1(b) [Fig. 1(a)]. E_{APbI3} represents the energy of the reference system, which is either α-phase $APbI_3$ (A = MA, Cs, Rb, K), δ-phase $APbI_3$ as shown in Fig. 1(d), or products of decomposition, $AI + PbI_2$, in Fig. 1(e). The comparisons of total energies between α-phase $APbI_3$, δ-phase $APbI_3$, and $AI + PbI_2$ are shown in Table S1 of the Supplemental Material [36]. Similarly, for triple-cation FA-based perovskite $Cs_xMA_yFA_{(1-x-y)}PbI_3$, E_{rel} is calculated by Eq. (2):

$$E_{\mathrm{rel}} = E(x,y) - xE_{\mathrm{CsPbI3}} - yE_{\mathrm{MAPbI3}} - (1-x-y)E_{\mathrm{FAPbI3}}, \qquad (2)$$

where $E(x, y)$ is the total energy of the alloy $Cs_xMA_yFA_{(1-x-y)}PbI_3$, and x and y are doping concentrations for Cs and MA cations. The data of relative energy diagram of $Cs_xMA_yFA_{(1-x-y)}PbI_3$ is shown in Table S6 of the Supplemental Material [36]. The effect of configuration entropy on the diagram can be found in Fig. S3 and corresponding data as shown in Table S2 of the Supplemental Material [36].

Figures 2(a)–2(g) show the calculated relative energies of various double-cation perovskites $A_xFA_{(1-x)}PbI_3$ and

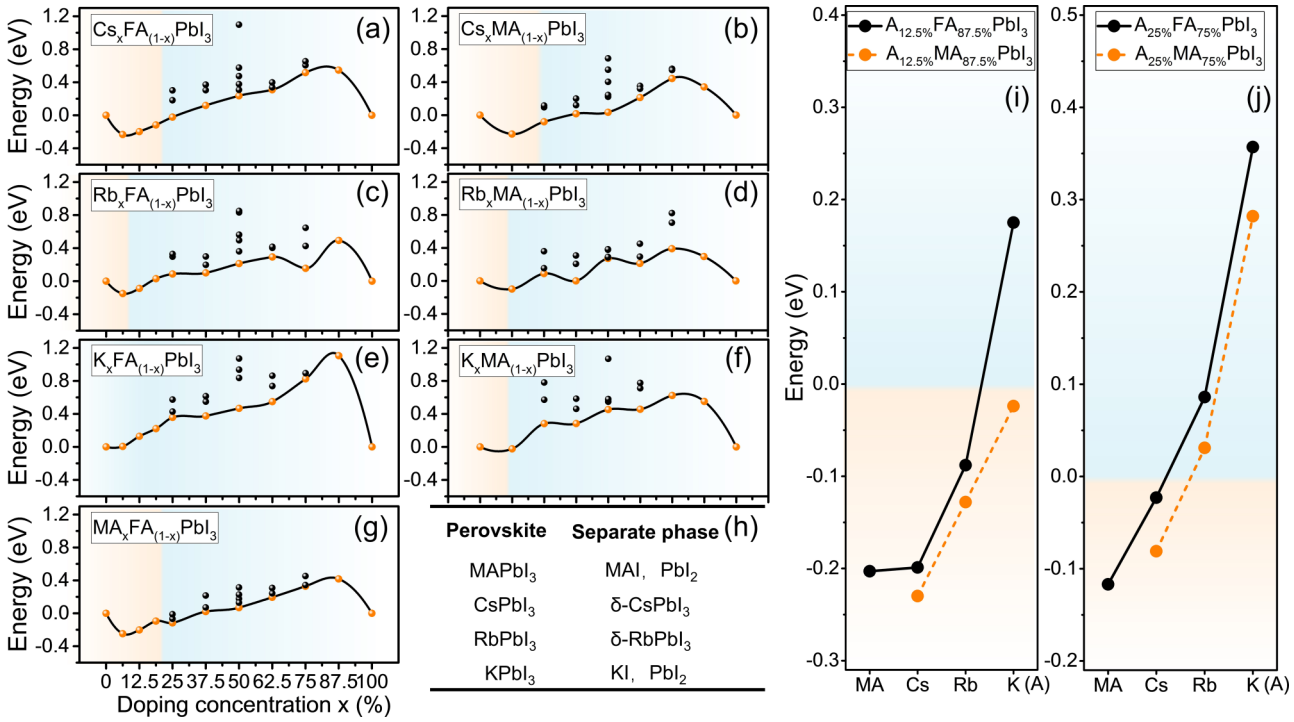

FIG. 2. Relative energy results for double-cation lead iodide perovskites. (a)–(g) The relative energies of various double-cation lead iodide perovskites with varying doping concentrations x. The spheres are the calculated relative energies for different configurations, with the yellow ones representing the most stable structures at each x and black ones representing other structures with higher energies. (h) The reference phases employed at the $x = 1$ limit. The lowest relative energies of mixed-cation structures doped by Cs, Rb, and K are obtained when x equals (i) 12.5% and (j) 25%, respectively.

$A_xMA_{(1-x)}PbI_3$. A negative value of relative energy indicates that the corresponding structure is thermodynamically more stable compared with the control and reference systems, whereas positive values indicate phase instability and segregation [37,38]. A general trend has been found that uniform doping is more likely to be achieved when the alloying ratio x is small, as indicated by the pale yellow region in Fig. 2. When more A cation is incorporated into the lattice, phase segregation to δ-$APbI_3$ or AI would occur. As shown in Figs. 2(a)–2(g), three kinds of systems most susceptible to uniformly doping are $Cs_xFA_{(1-x)}PbI_3$, $MA_xFA_{(1-x)}PbI_3$, and $Cs_xMA_{(1-x)}PbI_3$, which is consistent with our experimental results below.

The miscibility of various cations in FA/MA-based perovskites is related to the radius differences between dopants and FA/MA. We summarize the relative energies of different mixed-cation systems with $x = 12.5\%$ and 25% [Figs. 2(i) and 2(j)]. This result shows a miscible MA/FA or Cs/FA binary systems and phase segregation in K-doped lead halide perovskites. With larger radius, the cation is more likely to be incorporated into the $FAPbI_3/MAPbI_3$ lattices. Due to the large radius difference between K and FA/MA, the phase segregation is the most pronounced.

In addition to the miscibility, poor phase stability (compared with the δ phase) also limits the applications of OIHPs. To study the effect of doping on the phase stability of the perovskite structure, we calculated total energy differences between α-phase and δ-phase ($\Delta E_{\alpha\delta}$) for MA/Cs/Rb doping, as shown in Table I. For pure $FAPbI_3$, the $\Delta E_{\alpha\delta}$ is 0.03 eV, indicating a slight instability of the perovskite-phase $FAPbI_3$. The $\Delta E_{\alpha\delta}$ value becomes negative after MA/Cs/Rb doping increases to 12.5%, in which Rb is the most effective to stabilize the perovskite phase. But excess doping (as much as 25%) has an adverse effect on stabilizing the perovskite structure. It should also be noted that choosing different functionals will only change the values of $\Delta E_{\alpha\delta}$. The trend regarding the influence of dopants on the α-phase stability remains the same, as see in Table S3 of the Supplemental Material [36].

B. High-throughput experimentation

To corroborate the calculation results, we utilize robot-based high-throughput experimentation to automatically map the phase stability of mixed-cation $FAPbI_3$-based perovskites annealed at 90 °C. The setup is shown in Fig. 3, by which 144 samples were synthesized on homemade grid plates, including standard stoichiometric (SSt) and overstoichiometric (OSt with excess organic salt) ones. The robot starts with some other solutions, including $FAPbI_3$, $CsPbI_3$, MAI, CsI,

TABLE I. The calculated relative energies of α phase with respect to δ phase ($\Delta E_{\alpha\delta} = E_\alpha - E_\delta$) for $A_xFA_{(1-x)}PbI_3$ with optB86b-vdW functional.

Ratio (%)	MA^+	Cs^+	Rb^+	K^+
$X = 0$	0.030	0.030	0.030	0.030
$X = 12.5$	−0.110	−0.117	−0.142	−0.129
$X = 25$	0.112	0.135	0.116	0.110

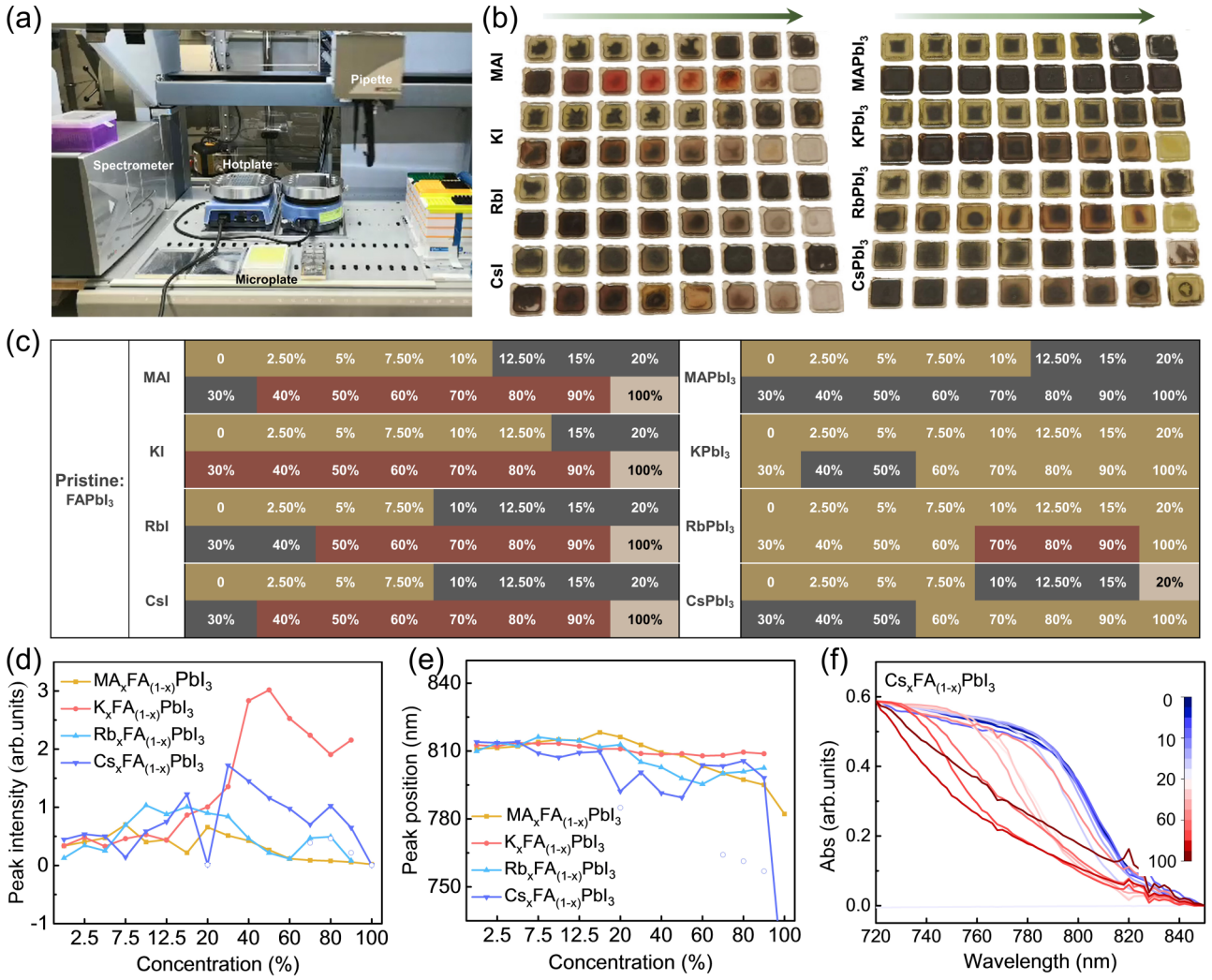

FIG. 3. High-throughput experiments. (a) Photograph of the high-throughput robotic system, including four automatic pipettes, spectrometer, hotplate. The samples are fabricated on glass located at the hotplate and then transferred to the analytic spectrometer. (b) Photographs and (c) corresponding composition table of $FAPbI_3$-based experimental samples including OSt (left, *AI* as dopant) and SSt (right, $APbI_3$ as dopant) ones. Every two rows correspond to one doping method. (d) The PL intensity and (e) PL peak position of MA/K/Rb/Cs-doped $FAPbI_3$ with varying doping concentrations at SSt condition; solid circles represent the splitting point for PL peak of $CsPbI_3$-doped perovskites. (f) Absorption spectrum of $CsPbI_3$-doped $FAPbI_3$ with varying doping content.

etc., followed by an automatic process to prepare the desired precursors (e.g., $Cs_{0.1}FA_{0.9}PbI_3$). The mixed precursors wobble for 10 min before depositing the perovskite layer on glass substrates via drop casting. First, we observed a general trend of color change from light yellow to gray (light yellow → black → gray) when the doping ratio increases from 0% to 100%, except for the $MAPbI_3$ system due to the black color of $MAPbI_3$. The transition from light yellow to black indicates a δ-α transition at a critical alloying ratio [see Figs. 3(b) and 3(c)], which is consistent with our simulation results in Table I. Further increase of the alloying ratio leads to formation of a nonperovskite phase for MA/K/Rb/Cs, which can be attributed to the phase instability and segregation.

We also noted that the stoichiometric ratio affects the resulting phase of these compounds. For OSt samples, RbI is the most efficient one to stabilize the perovskite phase compared with CsI/MAI [black region in Fig. 3(b)], while KI shows little effect, most likely because K cannot be doped into $FAPbI_3$. For the SSt sample, $CsPbI_3$ is the most effective one; moreover, $KPbI_3$ can also stabilize the perovskite phase for 40/50 mol % doping, although K is not expected to alloy with $FAPbI_3$. We reason that introduced $KPbI_3$ could act as a matrix to increase the bulk strain of interior $FAPbI_3$, leading to the formation of black-phase $FAPbI_3$. Interestingly, the rest of the yellow-phase $FAPbI_3$ cannot convert to black phase even if it is annealed at 160 °C, in contrast to $FAPbI_3$ fabricated by the spin-coating method (with antisolvent), which may indicate a different strain in these samples [39]. The samples fabricated by the drop-casting method are expected to contain a lower strain inside due to a slower growth rate with the resulting ~20 μm grain size (see Fig. S6a in the Supplemental Material [36]). We also observed that high humidity (approx. >35% RH) could turn the color of $MA_xFA_{(1-x)}PbI_3$ ($x <$ 10%) from partial yellow to full yellow, consistent with previous reports that high humidity degrades the perovskite phase

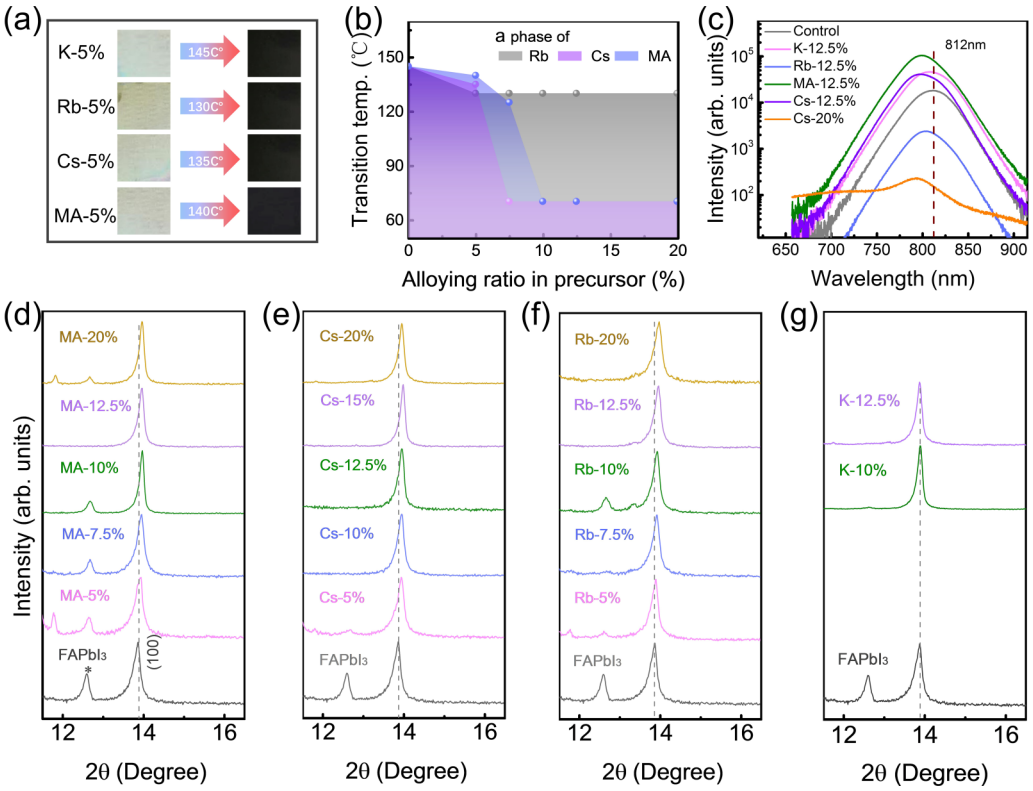

FIG. 4. Analysis of maximum alloying ratios. (a) Images of K/Rb/Cs/MA-doped $FAPbI_3$ with 5% molar ratio, after 90 °C annealing (left) and 130 °C–145 °C treatment (right). (b) The plot of transition temperature from δ phase to α phase for different cations. For Cs and MA, the transition temperature at 70 °C overestimates the real phase-transition temperature because 70 °C is the lowest temperature to remove solvent. (c) PL spectra of $FAPbI_3$ perovskite alloyed with varying ratios of K/Rb/Cs/MA. These samples were annealed at 150 °C/10 min before measurement. (d)–(g) XRD patterns of MA/Cs/Rb/K-doped $FAPbI_3$ after 150 °C/10 min annealing.

[40]. We note that the intrinsic phase diagram provides the basics for understanding mixed-cation perovskites, whereas many other external factors (e.g., humidity, strain) could also affect the phase-stable region and cation-miscibility region. We further analyzed the absorption and photoluminenscence (PL) data for these samples. Overall, PL intensity increases by cation engineering, although the optimal doping content varies for different cations [shown in Fig. 3(d)]. For low doping content, the enhanced PL intensity could relate to the improved crystal quality or boundary passivation. For the high doping content, the enhanced PL intensity might due to the formation of perovskite nanoparticles with a strong confinement effect inside the matrix of the secondary phase (e.g., $KI/KPbI_3/RbI/RbPbI_3$). From the trend of the peak position, all cation doping leads to a clear shift or splitting (e.g., Cs-doped perovskite at 20 mol %) of PL, except for K doping [see Fig. 3(e)]. Since theoretical simulations indicate that samples with doping content over 20 mol % should not present PL shift, the observed PL shift could be attributed to different film strains with the secondary phase. Figure 3(f) shows the influence of different $CsPbI_3$ contents on optical absorption properties. We can observe that the absorption spectra became more and more disordered at the band edge when doping content exceeds 20 mol %, a value which is close to the critical point of phase segregation we predicted above. The disordered absorption edge is observed for all the samples with high doping content, especially for K/Rb/Cs, which implies a disordered electronic structure or multiphase coexistence. In addition, the PL and absorption spectrum of other samples are shown in Fig. S4 of the Supplemental Material [36].

C. Analysis of maximum alloying ratio

We further fabricate perovskite films using spin coating in a glove box and examine the δ-α transition temperature in detail. $FAPbI_3$ is the control sample and $KPbI_3/RbPbI_3/CsPbI_3/MAPbI_3$ the dopant. With 5 mol % alloying, all films demonstrate white-yellow color after 70 °C annealing, indicating δ phase below this temperature. We found that the transition temperature is around 145 °C/130 °C/135 °C/140 °C, for $K_{0.05}/Rb_{0.05}/Cs_{0.05}/MA_{0.05}FA_{0.95}PbI_3$, respectively [abbreviated as K-5 mol %, Rb-5 mol %, Cs-5 mol %, MA-5 mol %, as shown in Fig. 4(a)]. The transition temperature of control sample $FAPbI_3$ is 145 °C. Compared with Cs/MA, Rb is the most efficient one in stabilizing the perovskite phase with the lowest transition temperature, while K has a negligible effect on changing transition temperature, which is consistent with our theoretical result suggesting that K cannot be uniformly mixed into $FAPbI_3$. With the doping ratio increases, Cs-7.5 mol % and MA-10 mol % become stable in perovskite phase at 70 °C [70 °C is the lowest temperature to remove solvent, as shown in Fig. 4(b)]; however, the transition temperature of Rb-10 mol % and Rb-20 mol % still

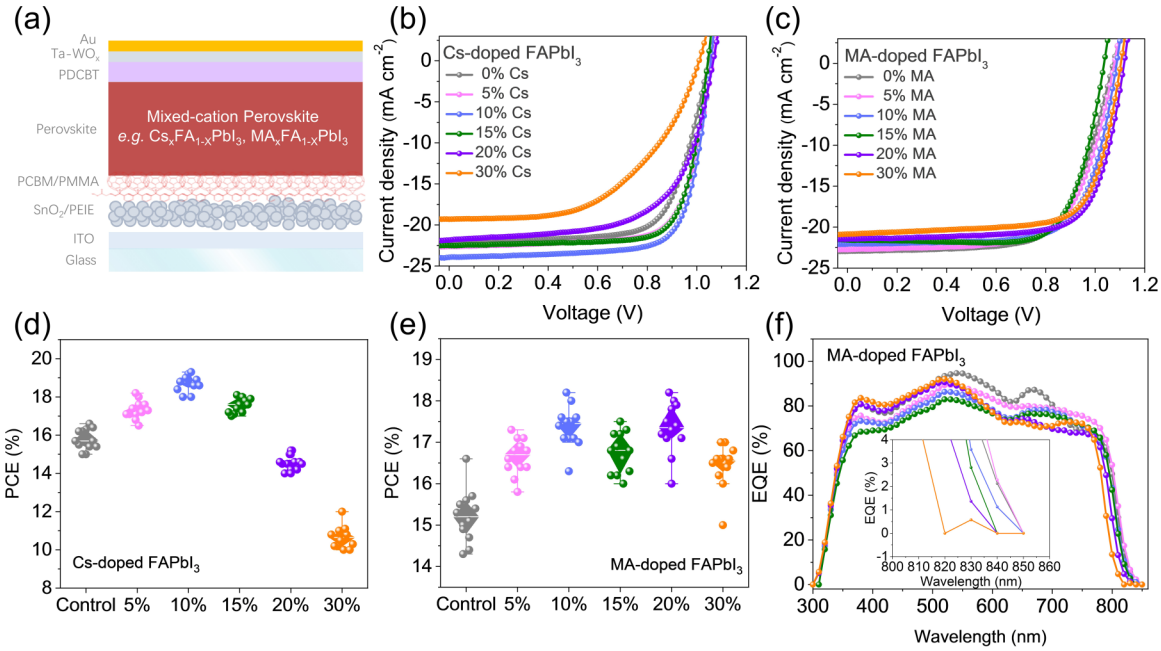

FIG. 5. Device characterization of mixed-cation perovskite solar cells. (a) Schematic representation of perovskite device structure used in this work. Current-voltage (J-V) curves of (b) $Cs_xFA_{(1-x)}PbI_3$ and (c) $MA_xFA_{(1-x)}PbI_3$ perovskite solar cells with different doping ratios. Statistics of power conversion efficiencies (PCE) of (d) $Cs_xFA_{(1-x)}PbI_3$ and (e) $MA_xFA_{(1-x)}PbI_3$ with various compositions. (f) External quantum efficiency (EQE) of $MA_xFA_{(1-x)}PbI_3$ with various compositions.

remains at 130 °C, which indicates a maximum alloying ratio of ∼5 mol % for Rb.

In order to further examine the maximum alloying ratio from experiments, we also analyzed the PL and XRD patterns in detail in Figs. 4(c) and 4(d)–4(g). In Fig. 4(c), all samples show a blue shift in PL spectra, except for K-12.5 mol %. In Figs. 4(d)–4(f), the peaks of (100) surface for MA/Cs/Rb doping present obviously shift with varying degrees, while a negligible shift is observed for K-doped $FAPbI_3$ in Fig. 4(g), again evidencing failed doping of K. More complete XRD and PL data are given in the Supplemental Material, see Table S4 and Fig. S5 [36]. Combined with the transition-temperature measurements above, we conclude that the maximum alloying ratio for K/Rb/Cs is ∼0 mol %, 5 mol %, and 12.5 mol %, respectively, in agreement with our calculation results.

To apply these results to devices, we fabricated perovskite solar cells with mixed-cation perovskites (i.e., $Cs_xFA_{(1-x)}PbI_3$, $MA_xFA_{(1-x)}PbI_3$). The device structure and performance are presented here as Fig. 5. In Figs. 5(b)–5(e), the highest efficiency is achieved by appropriate alloying of $FAPbI_3$ with MA or Cs, which is located at the region where the phase-stable and phase-pure perovskites can form. Lower MA/Cs content cannot fully eliminate the δ-phase $FAPbI_3$, while higher MA/Cs content leads to phase segregation (immiscible region). As shown in the external quantum efficiency (EQE) [Fig. 5(f) and Supplemental Material Fig. S6b [36]], >20 mol % Cs doping will not push the band edge toward lower wavelength anymore. For 30 mol % MA doping, it is interesting to observe a bump at around 830 nm in addition to the second rise at 815 nm [Fig. 5(f)], which clearly indicates certain phase segregation. The statistics of EQE, short circuit current (J_{sc}), fill factor (FF), and open-circuit voltage (V_{oc}) of the $Cs_xFA_{(1-x)}PbI_3$, $MA_xFA_{(1-x)}PbI_3$ with various compositions and scanning electron microscopy (SEM) of drop-casting film are shown in the Supplemental Material, Fig. S6 [36].

D. Finite-temperature (T) effect and phase diagram

To investigate the finite-temperature effect on stability and miscibility from a theoretical perspective, we plotted the phase diagram of a sample system $Cs_xFA_{(1-x)}PbI_3$, which could provide more insight for future experimental studies. Finite temperature would affect the entropy S (configuration and vibrational terms) and alloy internal energy U (probabilities of various alloy structures) and therefore change the Helmholtz free energy (F) and the thermodynamics properties of an alloy. First, the vibrational entropies of various alloys at room temperature (300 K) were calculated with density functional perturbation theory. The results are shown in the Supplemental Material, Table S5 [36], which suggests that vibrational entropy does not play a significant role in the phase stability of alloys. Then, we evaluate the influence of finite temperature on the configuration entropy and internal energy by using a statistical method, the generalized quasichemical approximation (GQCA) method. This method was used to calculate the thermodynamic properties at a wide range of chemical compositions and at arbitrary temperature. More calculation details about the GQCA method are summarized in the computational methods part of the Supplemental Material. The calculated ΔU, $T\Delta S$, and ΔF at various temperatures are shown in Fig. S3 of the Supplemental Material [36]. Based on the temperature-dependent ΔF curves, we then built the T-x phase diagram of $Cs_xFA_{(1-x)}PbI_3$ and show it in Fig. 6(a). The phase diagram shows that the critical temperature (T_c) is 734 K, above which the solid solution of any

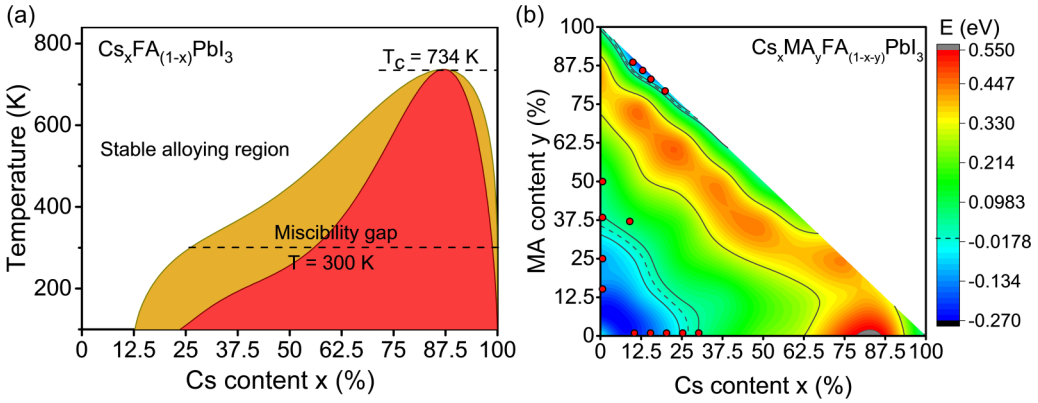

FIG. 6. Calculated phase diagram of $Cs_xFA_{(1-x)}PbI_3$ and relative energy diagram of $Cs_xMA_yFA_{(1-x-y)}PbI_3$. (a) T-x phase diagram of the $Cs_xFA_{(1-x)}PbI_3$ alloy. The red and yellow regions correspond to the unsteady and metastable states enclosed by the spinodal line and binodal lines, respectively, while the white region is the thermodynamically stable solid solution. (b) Relative energy diagram of triple-cation perovskite $Cs_xMA_yFA_{(1-x-y)}PbI_3$. The horizontal and vertical coordinates represent the doping proportion of Cs and MA, respectively. The red dots represent several reported multication perovskite compositions with good solar cell performance and stability from literature. Dashed lines indicate regions with zero relative energy.

composition is fully miscible and stable. A broad miscibility gap exists at room temperature and lower temperature, indicating a high tendency for segregation. The miscibility gap decreases with the increase of T. The calculated T-x phase diagram provides a more realistic model to understand the phase stability and segregation of mixed-cation lead iodide perovskites, and clearly rationalizes the observed maximum cation alloying ratios in both of previous [31] and our experiments.

We went one step further to study the phase stability and segregation of triple-cation perovskite beyond the double-cation cases. Because MA/Cs dopants are more compatible with $FAPbI_3$ lattice, we consider the case of $Cs_xMA_yFA_{(1-x-y)}PbI_3$. The relative energy diagrams are illustrated in Fig. 5(b), which shows the relative energies within the range of $x + y \leqslant 1$. There are two regions for stable triple-cation structures. The lower blue part indicates the FA-based structures with Cs and MA dopants, while the upper blue part denotes the MA-based structures with Cs doping. We have searched for reported FA- and MA-based mixed-cation perovskites with excellent photovoltaic efficiency and good stability in the literature [24,25,34,35,41–52]. As shown by red dots in Fig. 5(b), those stable mixed-cation perovskites with superb solar cell performances are mostly located in the two stable doping regions mentioned above. We also acknowledge that for the relative energy diagram of the triple-cation alloys, the calculation adopts a pseudocubic structure, although $MAPbI_3$ presents a tetragonal structure at room temperature. Through a literature search, we found that many experiments show that only a small concentration of Cs embedded in tetragonal-phase $MAPbI_3$ can help to maintain the structural stability [35], while excessive doping leads to phase segregation and phase transitions [34], which agrees well with our computational prediction. So our computational results are consistent with experiments and could provide strategies for further synthesizing stable FA- and MA-based mixed-cation perovskites in experiments.

III. CONCLUSION

Although the properties of OIHP-based solar cells greatly relies on compositional engineering (cation alloying), the understanding of phase stability and segregation of mixed-cation OIHP is still incomplete. Herein we investigated the phase stabilities and ideal doping concentrations of mixed-cation lead iodide perovskites and plotted out the phase diagram. *Ab initio* calculations and experiments show that among various kinds of ions (Cs^+, Rb^+, K^+, and MA^+), Cs^+ and MA^+ are more readily incorporated into the $FAPbI_3$ lattice due to their larger radii, while K^+ cannot be uniformly incorporated into the $FAPbI_3$ for any doping ratio x. Moderate amounts of Rb/Cs/MA dopants can help to stabilize the perovskite-phase (α-phase) structure. To convert δ phase to α phase above room temperature, over 10 mol % alloying is needed. Combining the discovered upper and lower limits of doping concentration, we restrict the appropriate alloying ratio to a very narrow region. Based on the calculated realistic T-x phase diagram, we analyze the segregation of mixed-cation lead iodide perovskites at varying T, which clearly rationalizes the experimentally observed maximum cation alloying ratio. We further generalize the ideal doping proportion in double-cation lead iodide perovskites to the triple-cation cases. The present work not only illustrates a universal thermodynamic understanding of phase stability and segregation of mixed-cation OIHPs but also provides insights and strategies for improving their photovoltaic performance.

ACKNOWLEDGMENTS

Y.F. is supported by the National Basic Research Programs of China under Grant No. 2016YFA0300900 and the National Science Foundation of China with Grants No. 11974105 and No. 11634001. Y.Z. acknowledges the Alexander von Humboldt Foundation for granting a Humboldt Fellowship

to support his scientific research during his postdoctoral work (Grant No. 1199604). The computational resources were provided by the computation platform of the National Super-Computer Center in Changsha, China.

[1] M. A. Green, Y. Hishikawa, E. D. Dunlop, D. H. Levi, J. Hohl-Ebinger, M. Yoshita, and A. W. Y. Ho-Baillie, Prog. Photovoltaics Res. Appl. **27**, 3 (2019).
[2] E. Cinquanta, D. Meggiolaro, S. G. Motti, M. Gandini, M. J. P. Alcocer, Q. A. Akkerman, C. Vozzi, L. Manna, F. De Angelis, A. Petrozza, and S. Stagira, Phys. Rev. Lett. **122**, 166601 (2019).
[3] R. Jinnouchi, J. Lahnsteiner, F. Karsai, G. Kresse, and M. Bokdam, Phys. Rev. Lett. **122**, 225701 (2019).
[4] W. J. Yin, T. Shi, and Y. Yan, Adv. Mater. **26**, 4653 (2014).
[5] T. Singh, A. Kulkarni, M. Ikegami, and T. Miyasaka, ACS Appl. Mater. Interfaces **8**, 14542 (2016).
[6] S. D. Stranks, G. E. Eperon, G. Grancini, C. Menelaou, M. J. P. Alcocer, T. Leijtens, L. M. Herz, A. Petrozza, and H. J. Snaith, Science **342**, 341 (2013).
[7] W.-J. Yin, J.-H. Yang, J. Kang, Y. Yan, and S.-H. Wei, J. Mater. Chem. A **3**, 8926 (2015).
[8] J. Kang and L. W. Wang, J. Phys. Chem. Lett. **8**, 489 (2017).
[9] Y. Feng, Y. Zhao, W.-K. Zhou, Q. Li, W. A. Saidi, Q. Zhao, and X.-Z. Li, J. Phys. Chem. Lett. **9**, 6536 (2018).
[10] A. Miyata, A. Mitioglu, P. Plochocka, O. Portugall, J. T.-W. Wang, S. D. Stranks, H. J. Snaith, and R. J. Nicholas, Nat. Phys. **11**, 582 (2015).
[11] V. D'Innocenzo, G. Grancini, M. J. Alcocer, A. R. Kandada, S. D. Stranks, M. M. Lee, G. Lanzani, H. J. Snaith, and A. Petrozza, Nat. Commun. **5**, 3586 (2014).
[12] G. R. Yettapu, D. Talukdar, S. Sarkar, A. Swarnkar, A. Nag, P. Ghosh, and P. Mandal, Nano Lett. **16**, 4838 (2016).
[13] T. Leijtens, S. D. Stranks, G. E. Eperon, R. Lindblad, E. M. J. Johansson, I. J. McPherson, H. Rensmo, J. M. Ball, M. M. Lee, and H. J. Snaith, ACS Nano **8**, 7147 (2014).
[14] M. Schlipf, S. Ponce, and F. Giustino, Phys. Rev. Lett. **121**, 086402 (2018).
[15] S. A. Veldhuis, P. P. Boix, N. Yantara, M. Li, T. C. Sum, N. Mathews, and S. G. Mhaisalkar, Adv. Mater. **28**, 6804 (2016).
[16] C. Fei, B. Li, R. Zhang, H. Fu, J. Tian, and G. Cao, Adv. Energy Mater. **7**, 1602017 (2017).
[17] T. Jesper Jacobsson, J.-P. Correa-Baena, M. Pazoki, M. Saliba, K. Schenk, M. Grätzel, and A. Hagfeldt, Energy Environ. Sci. **9**, 1706 (2016).
[18] M. Saliba, T. Matsui, K. Domanski, J.-Y. Seo, A. Ummadisingu, S. M. Zakeeruddin, J.-P. Correa Baena, W. R. Tress, A. Abate, A. Hagfeldt, and M. Grätzel, Science **354**, 206 (2016).
[19] J. Chang, H. Chen, H. Yuan, B. Wang, and X. Chen, Phys. Chem. Chem. Phys. **20**, 941 (2018).
[20] J. Chen, J. Xu, L. Xiao, B. Zhang, S. Dai, and J. Yao, ACS Appl. Mater. Interface **9**, 2449 (2017).
[21] S.-H. Turren-Cruz, A. Hagfeldt, and M. Saliba, Science **362**, 449 (2018).
[22] Y. Zhao, H. Tan, H. Yuan, Z. Yang, J. Z. Fan, J. Kim, O. Voznyy, X. Gong, L. N. Quan, C. S. Tan, J. Hofkens, D. Yu, Q. Zhao, and E. H. Sargent, Nat. Commun. **9**, 1607 (2018).
[23] Y. Zhao, Q. Li, W. Zhou, Y. Hou, Y. Zhao, R. Fu, D. Yu, X. Liu, and Q. Zhao, Sol. RRL **3**, 1800296 (2019).
[24] J. Huang, P. Xu, J. Liu, and X. Z. You, Small **13**, 1603225 (2017).
[25] P. Luo, S. Zhou, Y. Zhou, W. Xia, L. Sun, J. Cheng, C. Xu, and Y. Lu, ACS Appl. Mater. Interface **9**, 42708 (2017).
[26] J. Dai, Y. Fu, L. H. Manger, M. T. Rea, L. Hwang, R. H. Goldsmith, and S. Jin, J. Phys. Chem. Lett. **7**, 5036 (2016).
[27] O. A. Syzgantseva, M. Saliba, M. Gratzel, and U. Rothlisberger, J. Phys. Chem. Lett. **8**, 1191 (2017).
[28] Y. He, S. Q. Wang, X. X. Xue, L. Zhang, K. Chen, W. X. Zhou, and Y. Feng, J. Phys.: Condens. Matter **30**, 355501 (2018).
[29] M. Zhang, J. S. Yun, Q. Ma, J. Zheng, C. F. J. Lau, X. Deng, J. Kim, D. Kim, J. Seide, M. A. Green, S. Huang, and A. W. Y. Ho-Baillie, ACS Energy Lett. **2**, 438 (2017).
[30] Y. H. Park, I. Jeong, S. Bae, H. J. Son, P. Lee, J. Lee, C.-H. Lee, and M. J. Ko, Adv. Funct. Mater. **27**, 1605988 (2017).
[31] D. J. Kubicki, D. Prochowicz, A. Hofstetter, S. M. Zakeeruddin, M. Gratzel, and L. Emsley, J. Am. Chem. Soc. **139**, 14173 (2017).
[32] D. J. Kubicki, D. Prochowicz, A. Hofstetter, S. M. Zakeeruddin, M. Gratzel, and L. Emsley, J. Am. Chem. Soc. **140**, 7232 (2018).
[33] Z. Tang, S. Uchida, T. Bessho, T. Kinoshita, H. Wang, F. Awai, R. Jono, M. M. Maitani, J. Nakazaki, T. Kubo, and H. Segawa, Nano Energy **45**, 184 (2018).
[34] G. Gordillo Guzmán, C. F. Peña Camargo, and L. C. Luis Rincón, J. Alloys Compd. **750**, 286 (2018).
[35] R. G. Niemann, L. Gouda, J. Hu, S. Tirosh, R. Gottesman, P. J. Cameron, and A. Zaban, J. Mater. Chem. A **4**, 17819 (2016).
[36] See Supplemental Material at http://link.aps.org/supplemental/10.1103/PhysRevMaterials.4.095401 for (i) computational methods, (ii) experiment method, and (iii) additional discussion, including a theoretical and experimental part; also see [7,37,53–60].
[37] W. J. Yin, Y. Yan, and S. H. Wei, J. Phys. Chem. Lett. **5**, 3625 (2014).
[38] I. Kishida, K. Orita, A. Nakamura, and Y. Yokogawa, J. Power Sources **241**, 1 (2013).
[39] J. A. Steele, H. Jin, I. Dovgaliuk, R. F. Berger, T. Braeckevelt, H. Yuan, C. Martin, E. Solano, K. Lejaeghere, S. M. J. Rogge *et al.*, Science **365**, 679 (2019).
[40] J. Lin, M. Lai, L. Dou, C. S. Kley, H. Chen, F. Peng, J. Sun, D. Lu, S. A. Hawks, C. Xie, F. Cui, A. P. Alivisatos, D. T. Limmer, and P. Yang, Nat. Mater. **17**, 261 (2018).
[41] G. Zhou *et al.*, ACS Appl Mater. Interfaces **10**, 9503 (2018).
[42] J.-W. Lee, D.-H. Kim, H.-S. Kim, S.-W. Seo, S. M. Cho, and N.-G. Park, Adv. Energy Mater. **5**, 1501310 (2015).
[43] Z. Li, M. Yang, J.-S. Park, S.-H. Wei, J. J. Berry, and K. Zhu, Chem. Mater. **28**, 284 (2015).
[44] F.-X. Liang, J.-Z. Wang, Z.-X. Zhang, Y.-Y. Wang, Y. Gao, and L.-B. Luo, Adv. Opt. Mater. **5**, 1700654 (2017).
[45] C. Yi, J. Luo, S. Meloni, A. Boziki, N. Ashari-Astani, C. Grätzel, S. M. Zakeeruddin, U. Röthlisberger, and M. Grätzel, Energy Environ. Sci. **9**, 656 (2016).

[46] N. J. Jeon, J. H. Noh, W. S. Yang, Y. C. Kim, S. Ryu, J. Seo, and S. I. Seok, Nature (London) **517**, 476 (2015).
[47] A. Binek, F. C. Hanusch, P. Docampo, and T. Bein, J. Phys. Chem. Lett. **6**, 1249 (2015).
[48] D. Prochowicz, P. Yadav, M. Saliba, M. Saski, S. M. Zakeeruddin, J. Lewiński, and M. Grätzel, Sustainable Energy Fuels **1**, 689 (2017).
[49] D. J. Kubicki, D. Prochowicz, A. Hofstetter, P. Pechy, S. M. Zakeeruddin, M. Gratzel, and L. Emsley, J. Am. Chem. Soc. **139**, 10055 (2017).
[50] X. He, P. Guo, J. Wu, Y. Tu, Z. Lan, J. Lin, and M. Huang, Sol. Energy **157**, 853 (2017).
[51] H. Choi, J. Jeong, H.-B. Kim, S. Kim, B. Walker, G.-H. Kim, and J. Y. Kim, Nano Energy **7**, 80 (2014).
[52] B. Slimi, M. Mollar, I. B. Assaker, I. Kriaa, R. Chtourou, and B. Marí, Energy Procedia **102**, 87 (2016).
[53] W. Kohn and L. J. Sham, Phys. Rev. **140**, A1133 (1965).
[54] G. Kresse and J. Hafner, Phys. Rev. B **49**, 14251 (1994).
[55] J. P. Perdew, K. Burke, and M. Ernzerhof, Phys. Rev. Lett. **77**, 3865 (1996).
[56] F. Brivio, K. T. Butler, A. Walsh, and M. van Schilfgaarde, Phys. Rev. B **89**, 155204 (2014).
[57] A. Sher, M. van Schilfgaarde, A. B. Chen, and W. Chen, Phys. Rev. B **36**, 4279 (1987).
[58] L. K. Teles, J. Furthmüller, L. M. R. Scolfaro, J. R. Leite, and F. Bechstedt, Phys. Rev. B **63**, 085204 (2001).
[59] L. K. Teles, L. M. R. Scolfaro, J. R. Leite, J. Furthmüller, and F. Bechstedt, J. Appl. Phys. **92**, 7109 (2002).
[60] F. Brivio, C. Caetano, and A. Walsh, J. Phys. Chem. Lett. **7**, 1083 (2016).